Letter

Creation and manipulation of higher-order topological states by altermagnets

Yu-Xuan Li, Yichen Liu, and Cheng-Cheng Liu*

Center for Quantum Physics, Key Laboratory of Advanced Optoelectronic Quantum Architecture and Measurement (MOE), School of Physics, Beijing Institute of Technology, Beijing 100081, China

(Received 25 July 2023; revised 18 April 2024; accepted 22 April 2024; published 9 May 2024)

We propose to implement tunable higher-order topological states in a heterojunction consisting of a two-dimensional (2D) topological insulator and the recently discovered altermagnets, whose unique spin-polarization in both real and reciprocal space and null magnetization are in contrast to conventional ferromagnets and antiferromagnets. Based on symmetry analysis and effective edge theory, we show that the special spin splitting in altermagnets with different symmetries, such as d wave, can introduce Dirac mass terms with opposite signs on the adjacent boundaries of the topological insulator, resulting in the higher-order topological state with mass-domain-bound corner states. Moreover, by adjusting the direction of the Néel vector, we can manipulate such topological corner states by moving their positions. By first-principles calculations, taking a 2D topological insulator bismuthene with a square lattice on an altermagnet MnF_2 as an example, we demonstrate the feasibility of creating and manipulating the higher-order topological states through altermagnets. Finally, we discuss the experimental implementation and detection of the tunable topological corner states, as well as the potential non-Abelian braiding of the Dirac corner fermions.

DOI: 10.1103/PhysRevB.109.L201109

Introduction. Topological insulators (TIs), which have the helical edge states protected by time-reversal symmetry (TRS), set off an upsurge in topological matter research [1,2]. Recently, the introduction of higher-order topological states has expanded the topological matter research [3–34]. For the traditional first-order topological states like TIs, the difference between the dimensions of the topological boundary states and the bulk states is referred to as the codimension d_c which satisfies $d_c = 1$. In contrast, the higher-order topological states have a codimension d_c greater than one. For example, a second-order topological insulator in d dimensions exhibits the topologically protected hallmark boundary states of lower dimensionality $(d-2)$, such as corner states in two dimensions (2D) or hinge states in three dimensions (3D). Currently, only a few materials, such as SnTe [10], bismuth [9], $EuIn_2As_2$ [19], and $MnBi_{2n}Te_{3n+1}$ [28], are predicted to be 3D higher-order topological insulators (HOTIs). Experimental observation of the hinge states has so far been limited to bismuth [9,34]. As for 2D HOTIs, various candidates have been proposed [35–43], including hydrogenated and halogenated 2D hexagonal group-IV materials [35,36], Kekulé-ordered graphenes [35,44], 2D transition-metal dichalcogenides [37,38], and twisted moiré superlattices [39,40], but the experimental confirmation of their corner states is still lacking.

Usual approaches employed to achieve HOTI states include introducing a Zeeman field into a first-order TI [3,25,27,29] or harnessing the magnetic proximity effect to induce an exchange field within the TI [4,14,26,45]. However, in the existing approaches, the manipulation of the topological corner states (TCSs) is a big challenge, which impedes their potential application such as in quantum information processing [46–49].

In recent years, a new class of magnetic materials has emerged, known as altermagnets [50]. These materials exhibit collinear-compensated magnetic order, which goes beyond the traditional binary classification of ferromagnets and antiferromagnets. In altermagnets, the opposite spin sublattices are connected through rotation rather than inversion or translation, leading to nonrelativistic anisotropic spin splitting in the Brillouin zone. Experimentally, altermagnetism has been found in both metallic materials such as RuO_2 [50,51] and Mn_5Si_3 [52], and insulating materials such as MnF_2 [53,54] and MnTe [55]. The altermagnets have a unique spin splitting, leading to a wide range of fascinating phenomena [56–66], such as Andreev reflection [62], crystal Hall effect [54,63], finite-momentum Cooper pairs in altermagnet/superconductor heterojunctions [65], and topological superconductivity [51,64,67]. Given the features of altermagnets, an interesting question arises: can we utilize the novel altermagnets to create and manipulate the higher-order topological states?

In this work, we make a positive response to this question. Specifically, we design a heterostructure made of a TI and an altermagnet to create and manipulate the higher-order topological states, as illustrated in Fig. 1. By the effective model and edge theory, we find that when the in-plane Néel vector is around the $[1\bar{1}]$ direction, the original helical edge states protected by TRS are gapped with in-gap states localized at the two corners along the [11] direction, i.e., TCSs, as shown in Fig. 1. Furthermore, by changing the orientation of the Néel vector, we can effectively manipulate these TCSs. The two TCSs can be moved to the other two corners with the Néel vector rotated around the [11] direction. Based on first-principles calculations, we propose an experimental

*ccliu@bit.edu.cn

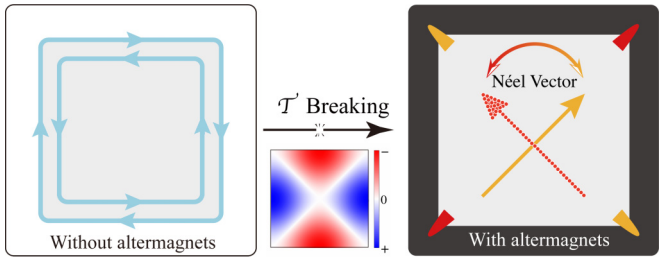

FIG. 1. Left panel: A 2D topological insulator with the helical edge states protected by time-reversal symmetry. Middle panel: A proximitized altermagnet induces altermagnetism in the 2D topological insulator and breaks time-reversal symmetry. We take a d-wave altermagnet as an example. Right panel: When the Néel vector lies in the plane, the helical edge states open a gap with two in-gap states localized at the corners appearing, i.e., the topological corner states (in orange). The manipulation of these corner states (in red) can be achieved by adjusting the Néel vector around the $[1\bar{1}]$ direction, as indicated by the red arrow.

setup that involves placing 2D buckled bismuth on the surface of the altermagnetic material MnF_2 [53,54] to realize and tune such TCSs. The magnetic proximity effect [45] plays a crucial role in inducing altermagnetism and spin splitting within the 2D TI. We confirm the existence of corner states in the MnF_2/Bi/MnF_2 sandwich structure and demonstrate the tunability of these TCSs. This intriguing setup provides a new platform for realizing non-Abelian statistics by using TCSs [46–49].

Model. We first introduce a first-order TI model defined on a square lattice with the Hamiltonian expressed in momentum space as

$$H_0(\boldsymbol{k}) = M(\boldsymbol{k})\sigma_z + A_x \sin k_x s_y \sigma_x - A_y \sin k_y s_x \sigma_x, \quad (1)$$

where $M(\boldsymbol{k}) = (m_0 - t_x \cos k_x - t_y \cos k_y)$, and σ_i and s_j are Pauli matrices acting on the orbital (a, b) and spin $(\uparrow, \downarrow)$ degree of freedom, respectively. The 2D TI protected by TRS $\mathcal{T} = is_y\mathcal{K}$, where $\mathcal{K}$ is the complex conjugate, and has inversion symmetry $\mathcal{P} = \sigma_z$. The $\mathcal{Z}_2$ topological invariants can be obtained from the parity eigenvalue on the time-reversal invariant momentum points Γ_i [68]. When $m_0^2 - (t_x + t_y)^2 < 0$ is satisfied, the TI with $\mathcal{Z}_2 = 1$ has TRS-protected helical edge states, as shown by the blue dashed line in Fig. 2(a).

The spin splitting of altermagnets exhibits various forms, including d wave, g wave, and i wave [50]. We take the proximity-induced d-wave spin splitting as an example which reads

$$H_{\mathrm{AM}}(\boldsymbol{k}) = 2J_0(\cos k_x - \cos k_y)\boldsymbol{s} \cdot \hat{\boldsymbol{n}}, \quad (2)$$

where the vector $\hat{\boldsymbol{n}} = (\sin\theta\cos\varphi, \sin\theta\sin\varphi, \cos\theta)$ represents the direction of the Néel vector. Here the in-plane Néel component $(\theta = \pi/2)$ is considered with the out-of-plane component left in the Supplemental Material (SM) [69]. As shown in Fig. 2(a), the original gapless helical edge states develop a gap when the in-plane Néel vector aligns along the $[1\bar{1}]$ direction. We further calculate the energy spectrum of a finite-size square sample, as displayed in the inset of Fig. 2(b). One can observe that two in-gap states emerge in the edge gap. We plot the wave-function distribution of these

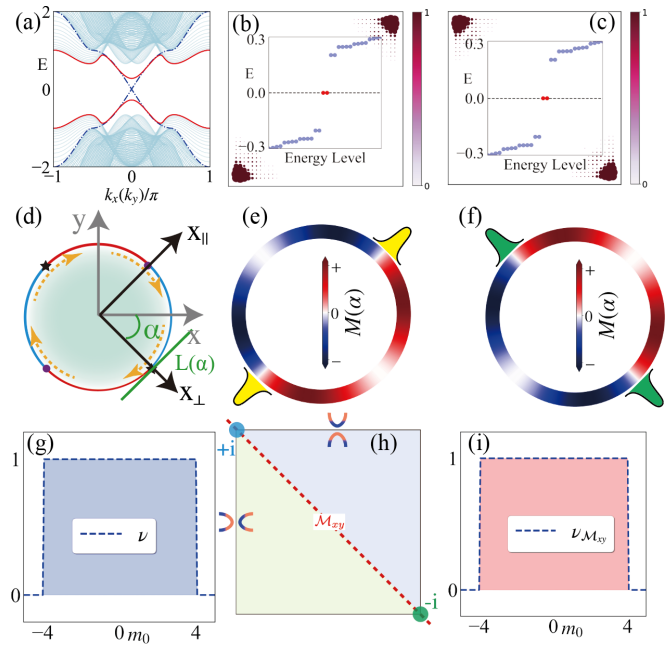

FIG. 2. (a) The edge spectrum for a cylinder geometry. The blue dotted lines represent the gapless helical edge states of the topological insulator. The red solid lines denote the gapped helical edge states after the altermagnet is turned on. (b) Inset: Two in-gap states emerge with the Néel vector along the $[1\bar{1}]$ direction. The real spatial distribution of their wave function is plotted. (c) Same as (b) but with the Néel vector along the [11] direction. (d) The tangents $L(\alpha)$, on which we will develop the generic edge theory, mark different boundaries with the clockwise rotation angle α. (e), (f) The change of the boundary Dirac mass with the rotation angle α when the Néel vector is along the $[1\bar{1}]$ direction and the [11] direction, respectively. (g) The topological invariant ν is plotted as a function of the m_0. (h) Schematic diagram: The boundary of the mirror-symmetry operation connection has opposite Dirac mass, and the TCSs originate from different mirror subspaces. (i) The mirror-graded winding number $\nu_{\mathcal{M}_{xy}}$ is plotted as a function of the m_0. Common parameters: $m_0 = 1.0, t_x = t_y = A_x = A_y = 2.0, J_0 = 0.5$.

in-gap states and find them to be localized at two corners of the square sample, as depicted in Fig. 2(b), which means the two localized in-gap states are possible TCSs. This provides evidence for the presence of the HOTI state in the system when altermagnetism is activated, indicating a topological phase transition from a first-order TI to a HOTI state.

When the Néel vector is directed along the [11] direction, the system also exhibits the HOTI states with the hallmark TCSs but on the other corners, as depicted in Fig. 2(c). Notice that more TCSs can be obtained with Néel vector along other directions or by altermagnets with higher angular momentum quantum numbers, such as g-wave and i-wave [69]. Therefore, by rotating the orientation of the Néel vector, we offer an effective method to manipulate the TCSs, enabling dynamic control and repositioning of these states within the system. In practical experiments, the orientation of the Néel vector can be controlled by applying an electric field or a spin-orbit torque [70–72]. Thus, this proposal opens up new possibilities for realizing non-Abelian statistics of Dirac fermions with fractional charge [48].

Symmetry analysis and edge theory. Our proposed model exhibits $C_{2z}T = s_x\mathcal{K}$ symmetry and falls within the Stiefel-Whitney (SW) class with its topology characterized by the second SW number w_2 [73,74]. Applying a unitary transformation $U = \exp(i\pi/4 s_x)$ to $H(\boldsymbol{k}) = H_0(\boldsymbol{k}) + H_{\mathrm{AM}}(\boldsymbol{k})$, a real form can be obtained [69]. We calculate the SW number w_2 by using the Wilson loop method with $w_2 = 1$, signifying a nontrivial HOTI [69].

The centrosymmetric topological insulator we consider has particle-hole-symmetric energy bands and thus can be considered to have chiral symmetry $\mathcal{C}$ approximately [26,29]. The introduction of altermagnetsim into the topological insulator breaks $\mathcal{T}$, while $\mathcal{P}$ and $\mathcal{C}$ remain intact. Such higher-order topological states belong to the $\mathbb{Z}_2$ classification [16]. The topological invariant characterizing the higher-order topology reads as $\nu = \sum_{\Gamma_i} n^-(\Gamma_i)/2 \mod 2$, where $n^-(\Gamma_i)$ is the number of occupied states with negative parity eigenvalue at time-reversal invariant points Γ_i. We calculate the topological invariant ν, as shown in Fig. 2(g), and $\nu = 1$ with $m_0 \in (-4, 4)$ indicates a HOTI.

The origin of these TCSs and their tunability in real space as the Néel vector changes can be understood through the edge theory. We use the Hamiltonian $H(\boldsymbol{k}) = H_0(\boldsymbol{k}) + H_{\mathrm{AM}}(\boldsymbol{k})$ to describe the HOTI. Expanding $H(\boldsymbol{k})$ at $\boldsymbol{\Gamma} = (0, 0)$ to the second order yields

$$H^{\mathrm{eff}}(\boldsymbol{k}) = \left(m + \frac{t_x}{2}k_x^2 + \frac{t_y}{2}k_y^2\right)\sigma_z + A_x k_x \sigma_x s_y - A_y k_y \sigma_x s_x - J_0\left(k_x^2 - k_y^2\right)\boldsymbol{s}\cdot\hat{\boldsymbol{n}}, \tag{3}$$

where $m = m_0 - t_x - t_y$. We consider an arbitrary boundary $L(\alpha)$, which is the tangent with the clockwise rotation angle α, as shown in Fig. 2(d). The coordinate axes need to be rotated to obtain the new momentum $k_\parallel$ and $k_\perp$. In the new coordinates, when the strength of the altermagnets is smaller than the bulk gap, the Hamiltonian can be decomposed as $H^{\mathrm{eff}}(\boldsymbol{k}) = H_0(\boldsymbol{k}) + H_p(\boldsymbol{k})$ (see details in the SM [69]). Consider the semi-infinite plane $x_\perp \in (-\infty, 0]$, where a boundary exists at $x_\perp = 0$. The momentum $k_\perp$ is replaced by $-i\partial_\perp$ and the eigenequation $H_0\psi_\alpha(x_\perp) = E_\alpha\psi(x_\perp)$ is solved with the boundary condition $\psi(0) = \psi(-\infty) = 0$. Two solutions for $E_\alpha = 0$ are obtained with $\psi_\alpha(x_\perp) = \mathcal{N}_\perp \sin(\kappa_1 x_\perp)e^{\kappa_2 x_\perp}e^{ik_\parallel x_\parallel}\chi_\alpha$, where the normalization constant is given by $|\mathcal{N}_\perp|^2 = 4|\kappa_2(\kappa_1^2 + \kappa_2^2)/\kappa_1^2|$ and the eigenvector χ_α satisfies $(\sin\alpha s_y + \cos\alpha s_x)\sigma_y\xi = \xi$. We choose χ_i as $\chi_1 = 1/\sqrt{2}(-ie^{-i\alpha}, 0, 0, 1)^T$ and $\chi_2 = 1/\sqrt{2}(0, ie^{-i\alpha}, 1, 0)^T$ and project perturbation H_p onto the bases (ψ_1, ψ_2), and obtain the boundary Hamiltonian for any boundary $L(\alpha)$ and any Néel vector with polar θ and azimuthal φ angles

$$H_{\mathrm{eff}}(x_\perp, k_\parallel) = Ak_\parallel\eta_z + M(\alpha, \theta, \varphi)\eta_y, \tag{4}$$

where η_i are Pauli matrices acting on ψ_i.

The Dirac mass term that arises from altermagnets is given by

$$M(\alpha, \theta, \varphi) \sim J_0 \sin\theta\cos(2\alpha)\cos(\varphi - \alpha). \tag{5}$$

Our research primarily concentrates on the in-plane component of the Néel vector with $\theta = \pi/2$, while the out-of-plane component of the Néel vector does not influence the edge states (see details in the SM [69]). For the scenario that the Néel vector is along the $[\bar{1}1]$ direction ($\varphi = 3\pi/4$), we calculate and plot the Dirac mass at any edge $L(\alpha)$, as depicted in Fig. 2(e). One can observe that at the clockwise rotation angles of $\alpha = 3\pi/4$ and $7\pi/4$, there exist domains in the Dirac mass that host zero-energy bound states resembling Jackiw-Rebbi zero modes [75], which is consistent with the numerical results of a square sample shown in Fig. 2(b). Although the Dirac mass $M(\alpha)$ vanishes at $\alpha = \pi/4$ and $5\pi/4$, the lack of a mass domain prevents the formation of the TCSs. When the Néel vector is aligned with the [11] direction, two mass domains are formed at $\alpha = \pi/4$ and $5\pi/4$, respectively, as plotted in Fig. 2(f). The two TCSs can be moved by rotating the Néel vector. Consequently, we cannot only create TCSs but also manipulate them by an altermagnet.

It is worth noting that when the Néel vector is along the [11] direction, the system has extra mirror symmetry $\mathcal{M}_{xy} = i\sqrt{2}/2(s_x + s_y)$ along a line defined by $k_x = -k_y$. Along the mirror-invariant line, the Hamiltonian $H(\boldsymbol{k}) = H_0(\boldsymbol{k}) + H_{\mathrm{AM}}(\boldsymbol{k})$ can be decomposed into distinct mirror subspaces labeled by the $\pm i$. In each subspace, the Hamiltonian expressed as $\mathcal{H}^{\pm i} = \boldsymbol{q}_{\pm i}(k)\cdot\boldsymbol{\sigma}$, which are two 1D SSH models with opposite winding number $\nu_{+i} = -\nu_{-i}$ [69]. Intuitively, the nontrivial SSH model will result in two end states at an endpoint. However, when the Néel vector deviates from [11], mirror symmetry $\mathcal{M}_{xy}$ is broken, and the gap of the system is maintained. This indicates that regardless of the presence or absence of $\mathcal{M}_{xy}$, the system is in the same topological phase and has the $\mathbb{Z}_2$ classification [7,16], only one end state stable at one corner. As a result, the system will only exhibit two corner states instead of four. Furthermore, the chiral symmetry $\mathcal{C} = s_z\sigma_x$ which satisfies $\{\mathcal{M}_{xy}, \mathcal{C}\} = 0$ implies that the two corner zero modes originate from different mirror subspaces, as shown in Fig. 2(h). In the presence of mirror symmetry, the nontrivial second-order topology can currently be characterized by a mirror-graded winding number, which is defined as $\nu_{\mathcal{M}_{xy}} = (\nu_{+i} - \nu_{-i})/2$. A nonzero $\nu_{\mathcal{M}_{xy}}$ indicates that the system has a nontrivial second-order topology [76]. The calculated $\nu_{\mathcal{M}_{xy}}$ is shown in Fig. 2(i), which is consistent with Fig. 2(g), confirming the nontrivial topology of the system. The investigation of the Néel vector along $[1\bar{1}]$ is similar [69].

The TCSs still robustly exist when the Néel vector deviates from the [11] or $[1\bar{1}]$ direction. As long as the condition $M(\alpha, \pi/2, \varphi)M(\alpha + \pi/2, \pi/2, \varphi) < 0$ or $M(\alpha, \pi/2, \varphi)M(\alpha - \pi/2, \pi/2, \varphi) < 0$ is met, the system will have TCSs. Since $M(\alpha + \pi/2, \pi/2, \varphi) = -M(\alpha - \pi/2, \pi/2, \varphi)$, the condition is equivalent to $M(\alpha, \pi/2, \varphi)M(\alpha + \pi/2, \pi/2, \varphi) \neq 0$, i.e., $\varphi \notin \{3\pi/2 - \alpha, \pi - \alpha, \pi/2 - \alpha, \alpha\}$. In principle, TCSs will exist as long as the condition holds. However, along these two directions $\varphi = \pi/4 - \alpha$ and $\varphi = 3\pi/4 - \alpha$, corresponding to [11] or $[1\bar{1}]$ directions with $\alpha = 0$, the edge gap is large, which is convenient for experimental observation of TCSs.

We also derive the general boundary Hamiltonian for the other anisotropic spin splittings with nonzero angular-momentum quantum numbers, such as g wave and i wave, and the isotropic spin splitting of s wave with zero angular momentum. The previous proposals to induce TCSs by using the Zeeman field can be considered as the special isotropic s-wave case in our proposal [69].

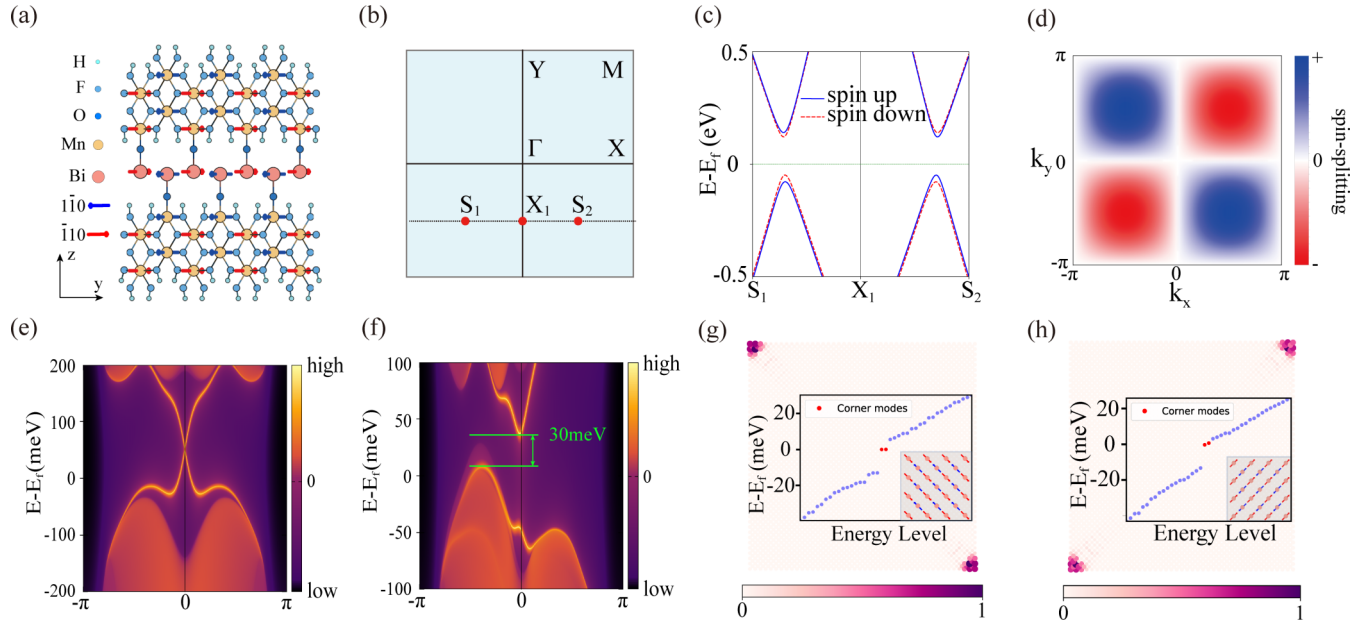

FIG. 3. (a) Side view of the optimized crystal structure of the $MnF_2/Bi/MnF_2$ configuration. (b) The 2D Brillouin zone with high-symmetric points and lines. (c) The spin-polarized energy bands of the $MnF_2/Bi/MnF_2$ sandwich structure, where the blue-solid/red-dashed lines represent the spin-up/spin-down. (d) The d-wave spin-polarized band splitting induced in bismuthene from our DFT calculation. (e) Helical edge states are calculated via DFT in the absence of altermangetism. (f) Gapped edge states obtained by the DFT calculation with the Néel vector aligned along the $[1\bar{1}]$ direction. (g) and (h) Néel vector along the $[1\bar{1}]$ and [11] directions, respectively. Inset: Two in-gap topological corner states emerge. The small arrows depict the direction of the Néel vector. The real spatial distribution of their wave function is plotted.

Material realization. Based on first-principles calculations, as a demonstration, we propose that a $MnF_2/Bi/MnF_2$ sandwich with optimized structure depicted in Fig. 3(a) can achieve such tunable TCSs (see details in the SM [69]). Previous studies have shown the potential of two-dimensional bismuthene, with its honeycomb lattice structure, to be used as a material for TIs [77–81]. And bismuthene has been successfully synthesized on SiC substrates [81]. To ensure lattice alignment between bismuthene and MnF_2, we utilize bismuthene with a buckled square lattice structure. This specific configuration of bismuthene, as a first-order TI, has an energy gap of approximately 0.69 eV [82], making it suitable for observing the TCSs. Through the magnetic proximity effect [45], magnetism can be induced in the buckled bismuthene. We employ a sandwich structure with $[C_2][S_4]$ symmetry where S_4 connects the sublattices with opposite spin in real space and C_2 inverse the spins in spin space [50], ensuring that the magnetic moment produced through the proximity effect satisfies the restriction of altermagnetism, as illustrated in Fig. 3(a). Based on first-principles density-functional theory (DFT) calculations, we present the spin-polarized energy bands in Fig. 3(c) (see details in the SM [69]). Notably, along a horizontal line ($S_1X_1S_2$) in the Brillouin zone, as shown in Fig. 3(b), the energy band exhibits the unique spin splitting with spin-up/down in blue-solid/red-dashed lines, demonstrating the characteristic behavior of d-wave spin splitting, as shown in Fig. 3(d). This spin splitting, approximately 30 meV, confirms the effective induction of altermagnetism in bismuthene through the magnetic-proximity effect.

To better investigate the electronic structure and topological properties, we construct an *ab initio* tight-binding model based on DFT and Wannier function [83,84]. The model can take into account the effect of altermagnetism in MnF_2. Additionally, we build a minimal tight-binding model based on symmetry to capture the physics of the DFT results [69]. In the absence of altermagnetism, we observe gapless edge states within the bulk gap of the buckled bismuthene, as shown in Fig. 3(e). However, by activating the altermagnetism of MnF_2 with the in-plane Néel vector along the diagonal direction, the helical edge states acquire a gap of approximately 30 meV, as shown in Fig. 3(f). A similar phenomenon is observed when the Néel vector is along the off-diagonal direction [69]. These indicate the breakdown of the first-order topology of the system and possibly the higher-order topology induced by the altermagnet. We calculate the energy spectrum of a finite-size square sample of the $MnF_2/Bi/MnF_2$ sandwich structure, as shown in Figs. 3(g) and 3(h). When the Néel vector has an in-plane component, it can be observed that two in-gap states emerge in red and the corresponding distribution of wave function is localized at two corners of the sample. Consequently, despite the altermagnetism causing the first-order topology of the system to be trivial, the system exhibits a nontrivial second-order topology. Moreover, the position of the corner states can be manipulated by rotating the Néel vector. This observation is consistent with our theoretical model results. Additionally, upon enabling spin-orbit coupling, the sandwich structure exhibits $C_{2z}T$ symmetry with its nontrivial second SW number w_2 confirmed via the Wilson loop method [69]. Therefore, by employing DFT calculations,

we demonstrate the capability to achieve and modulate the TCSs through manipulation of the Néel vector direction and provide a candidate material setup.

Discussion. Motivated by the unique spin-polarized band splitting in altermagnetic materials, we propose a route to create and manipulate TCSs by altermagnets. Our DFT calculations have confirmed that the magnetic proximity effect induces a spin-polarized band splitting in TIs and suggest a $MnF_2/Bi/MnF_2$ sandwich structure as a candidate material setup for realizing our proposal. The braiding of TCSs can be facilitated by constructing a cross-shaped or T-shaped geometry [85]. A gate electrode is positioned at the intersection point, allowing the generation and fusion of TCSs to be achieved by controlling the channel's opening and closing through gate voltage control [49]. Our proposal expands the possibility of TCS manipulation by controlling the Néel vector, which can employ gate-voltage control to enable more intricate braiding operations and pave the way for topological quantum computing. In the experiment, the direction of the Néel vector in altermagnets, like other antiferromagnetic materials, can be manipulated and detected using techniques such as current, voltage [71,86], strain [87,88], and spin-orbit torques [89]. Moreover, altermagnetic materials exhibit robustness to external magnetic-field perturbations, and their ultrafast response due to the absence of a coercivity field [90]. These fascinating properties open up the exciting possibility of achieving non-Abelian braiding of Dirac fermions [47–49], providing new avenues for future research and technological applications.

The existence of charged TCSs can be detected using scanning-tunneling microscopy (STM) [91]. Additional evidence for the presence of TCSs can be provided by exploiting the ability of the Néel vector to modulate the topological states. In the case where the Néel vectors are oriented along the z axis ($\theta = 0$), the system has gapless edge states. When the energy of the STM probe approaches that of the edge states, a broadening peak can be observed along the boundary. By adjusting the Néel vector to open a gap in the edge state, sharp peaks can be observed at the corners of the sample using STM. Consequently, the observation of changing energy-spectrum peaks with STM can serve as strong evidence for the existence of corner states. Furthermore, by manipulating the Néel vector, it is possible to control the movement of the corner states along the boundary and achieve a quantum charge pump independently of the bulk state [92]. This effect can be precisely measured through transport experiments, further supporting the understanding of the influence of the Néel vector on the topological properties of the system. The ability to control the movement of corner states and achieve a quantum charge pump holds potential implications for applications in quantum information processing and topological devices.

Note added. Recently, there appeared a related preprint [93] that focuses on the altermagnets and higher-order topology.

Acknowledgments. It is our pleasure to thank Shifeng Qian and Yongpan Li for their insightful discussions. The work is supported by the National Key & Program of China (Grant No. 2020YFA0308800), the NSF of China (Grant No. 12374055), and the Science Fund for Creative Research Groups of NSFC (Grant No. 12321004) Yu-Xuan Li and Yichen Liu contribute equally to the work.

[1] M. Z. Hasan and C. L. Kane, Rev. Mod. Phys. **82**, 3045 (2010).
[2] X.-L. Qi and S.-C. Zhang, Rev. Mod. Phys. **83**, 1057 (2011).
[3] M. Sitte, A. Rosch, E. Altman, and L. Fritz, Phys. Rev. Lett. **108**, 126807 (2012).
[4] F. Zhang, C. L. Kane, and E. J. Mele, Phys. Rev. Lett. **110**, 046404 (2013).
[5] W. A. Benalcazar, B. A. Bernevig, and T. L. Hughes, Science **357**, 61 (2017).
[6] W. A. Benalcazar, B. A. Bernevig, and T. L. Hughes, Phys. Rev. B **96**, 245115 (2017).
[7] J. Langbehn, Y. Peng, L. Trifunovic, F. von Oppen, and P. W. Brouwer, Phys. Rev. Lett. **119**, 246401 (2017).
[8] Z. Song, Z. Fang, and C. Fang, Phys. Rev. Lett. **119**, 246402 (2017).
[9] F. Schindler, Z. Wang, M. G. Vergniory, A. M. Cook, A. Murani, S. Sengupta, A. Y. Kasumov, R. Deblock, S. Jeon, I. Drozdov, H. Bouchiat, S. Guéron, A. Yazdani, B. A. Bernevig, and T. Neupert, Nat. Phys. **14**, 918 (2018).
[10] F. Schindler, A. M. Cook, M. G. Vergniory, Z. Wang, S. S. P. Parkin, B. A. Bernevig, and T. Neupert, Sci. Adv. **4**, eaat0346 (2018).
[11] J. Noh, W. A. Benalcazar, S. Huang, M. J. Collins, K. P. Chen, T. L. Hughes, and M. C. Rechtsman, Nat. Photon. **12**, 408 (2018).
[12] C.-H. Hsu, P. Stano, J. Klinovaja, and D. Loss, Phys. Rev. Lett. **121**, 196801 (2018).
[13] Q. Wang, C.-C. Liu, Y.-M. Lu, and F. Zhang, Phys. Rev. Lett. **121**, 186801 (2018).
[14] T. Liu, J. J. He, and F. Nori, Phys. Rev. B **98**, 245413 (2018).
[15] Z. Yan, F. Song, and Z. Wang, Phys. Rev. Lett. **121**, 096803 (2018).
[16] E. Khalaf, Phys. Rev. B **97**, 205136 (2018).
[17] M. Ezawa, Phys. Rev. Lett. **120**, 026801 (2018).
[18] J. Ahn, D. Kim, Y. Kim, and B.-J. Yang, Phys. Rev. Lett. **121**, 106403 (2018).
[19] Y. Xu, Z. Song, Z. Wang, H. Weng, and X. Dai, Phys. Rev. Lett. **122**, 256402 (2019).
[20] W. A. Benalcazar, T. Li, and T. L. Hughes, Phys. Rev. B **99**, 245151 (2019).
[21] X.-H. Pan, K.-J. Yang, L. Chen, G. Xu, C.-X. Liu, and X. Liu, Phys. Rev. Lett. **123**, 156801 (2019).
[22] Y. Peng and G. Refael, Phys. Rev. Lett. **123**, 016806 (2019).
[23] Y. Volpez, D. Loss, and J. Klinovaja, Phys. Rev. Lett. **122**, 126402 (2019).
[24] R.-X. Zhang, W. S. Cole, and S. Das Sarma, Phys. Rev. Lett. **122**, 187001 (2019).
[25] X. Zhu, Phys. Rev. B **97**, 205134 (2018).
[26] C. Chen, Z. Song, J.-Z. Zhao, Z. Chen, Z.-M. Yu, X.-L. Sheng, and S. A. Yang, Phys. Rev. Lett. **125**, 056402 (2020).

[27] Y.-J. Wu, J. Hou, Y.-M. Li, X.-W. Luo, X. Shi, and C. Zhang, Phys. Rev. Lett. **124**, 227001 (2020).

[28] R.-X. Zhang, F. Wu, and S. Das Sarma, Phys. Rev. Lett. **124**, 136407 (2020).

[29] Y. Ren, Z. Qiao, and Q. Niu, Phys. Rev. Lett. **124**, 166804 (2020).

[30] X. Wu, W. A. Benalcazar, Y. Li, R. Thomale, C.-X. Liu, and J. Hu, Phys. Rev. X **10**, 041014 (2020).

[31] T. Nag, V. Juričić, and B. Roy, Phys. Rev. B **103**, 115308 (2021).

[32] Y.-B. Yang, K. Li, L.-M. Duan, and Y. Xu, Phys. Rev. B **103**, 085408 (2021).

[33] E. Khalaf, W. A. Benalcazar, T. L. Hughes, and R. Queiroz, Phys. Rev. Res. **3**, 013239 (2021).

[34] T. Zhang, V. Sheina, S. Vlaic, S. Pons, D. Roditchev, C. David, G. Rodary, J.-C. Girard, and H. Aubin, Phys. Rev. B **108**, 085422 (2023).

[35] S. Qian, C.-C. Liu, and Y. Yao, Phys. Rev. B **104**, 245427 (2021).

[36] M. Pan, D. Li, J. Fan, and H. Huang, npj Comput. Mater. **8**, 1 (2022).

[37] S. Qian, G.-B. Liu, C.-C. Liu, and Y. Yao, Phys. Rev. B **105**, 045417 (2022).

[38] J. Zeng, H. Liu, H. Jiang, Q.-F. Sun, and X. C. Xie, Phys. Rev. B **104**, L161108 (2021).

[39] M. J. Park, Y. Kim, G. Y. Cho, and S. B. Lee, Phys. Rev. Lett. **123**, 216803 (2019).

[40] B. Liu, L. Xian, H. Mu, G. Zhao, Z. Liu, A. Rubio, and Z. F. Wang, Phys. Rev. Lett. **126**, 066401 (2021).

[41] X.-L. Sheng, C. Chen, H. Liu, Z. Chen, Z.-M. Yu, Y. X. Zhao, and S. A. Yang, Phys. Rev. Lett. **123**, 256402 (2019).

[42] Z. Guo, J. Deng, Y. Xie, and Z. Wang, npj Quantum Mater. **7**, 87 (2022).

[43] L. Wang, Y. Jiang, J. Liu, S. Zhang, J. Li, P. Liu, Y. Sun, H. Weng, and X.-Q. Chen, Phys. Rev. B **106**, 155144 (2022).

[44] H. Mu, B. Liu, T. Hu, and Z. Wang, Nano Lett. **22**, 1122 (2022).

[45] I. Vobornik, U. Manju, J. Fujii, F. Borgatti, P. Torelli, D. Krizmancic, Y. S. Hor, R. J. Cava, and G. Panaccione, Nano Lett. **11**, 4079 (2011).

[46] A.Yu. Kitaev, Ann. Phys. **303**, 2 (2003).

[47] J. Klinovaja and D. Loss, Phys. Rev. Lett. **110**, 126402 (2013).

[48] Y. Wu, H. Jiang, J. Liu, H. Liu, and X. C. Xie, Phys. Rev. Lett. **125**, 036801 (2020).

[49] Y. Wu, H. Liu, J. Liu, H. Jiang, and X. C. Xie, Natl. Sci. Rev. **7**, 572 (2020).

[50] L. Šmejkal, J. Sinova, and T. Jungwirth, Phys. Rev. X **12**, 031042 (2022).

[51] K.-H. Ahn, A. Hariki, K.-W. Lee, and J. Kuneš, Phys. Rev. B **99**, 184432 (2019).

[52] H. Reichlová, R. L. Seeger, R. González-Hernández, I. Kounta, R. Schlitz, D. Kriegner, P. Ritzinger, M. Lammel, M. Leiviskä, V. Petříček, P. Doležal, E. Schmoranzerová, A. Bad'ura, A. Thomas, V. Baltz, L. Michez, J. Sinova, S. T. B. Goennenwein, T. Jungwirth, and L. Šmejkal, arXiv:2012.15651.

[53] L.-D. Yuan, Z. Wang, J.-W. Luo, E. I. Rashba, and A. Zunger, Phys. Rev. B **102**, 014422 (2020).

[54] L. Šmejkal, R. González-Hernández, T. Jungwirth, and J. Sinova, Sci. Adv. **6**, eaaz8809 (2020).

[55] R. D. Gonzalez Betancourt, J. Zubáč, R. Gonzalez-Hernandez, K. Geishendorf, Z. Šobáň, G. Springholz, K. Olejník, L. Šmejkal, J. Sinova, T. Jungwirth, S. T. B. Goennenwein, A. Thomas, H. Reichlová, J. Železný, and D. Kriegner, Phys. Rev. Lett. **130**, 036702 (2023).

[56] H.-Y. Ma, M. Hu, N. Li, J. Liu, W. Yao, J.-F. Jia, and J. Liu, Nat. Commun. **12**, 2846 (2021).

[57] H. Bai, Y. C. Zhang, Y. J. Zhou, P. Chen, C. H. Wan, L. Han, W. X. Zhu, S. X. Liang, Y. C. Su, X. F. Han, F. Pan, and C. Song, Phys. Rev. Lett. **130**, 216701 (2023).

[58] S. Das, D. Suri, and A. Soori, J. Phys.: Condens. Matter **35**, 435302 (2023).

[59] S. A. A. Ghorashi, T. L. Hughes, and J. Cano, arXiv:2306.09413.

[60] J. A. Ouassou, A. Brataas, and J. Linder, Phys. Rev. Lett. **131**, 076003 (2023).

[61] M. Papaj, Phys. Rev. B **108**, L060508 (2023).

[62] C. Sun, A. Brataas, and J. Linder, Phys. Rev. B **108**, 054511 (2023).

[63] X. Zhou, W. Feng, R.-W. Zhang, L. Smejkal, J. Sinova, Y. Mokrousov, and Y. Yao, Phys. Rev. Lett. **132**, 056701 (2023).

[64] D. Zhu, Z.-Y. Zhuang, Z. Wu, and Z. Yan, Phys. Rev. B **108**, 184505 (2023).

[65] S.-B. Zhang, L.-H. Hu, and T. Neupert, Nature Commun. **15**, 1801 (2023).

[66] C. W. J. Beenakker and T. Vakhtel, Phys. Rev. B **108**, 075425 (2023).

[67] Y.-X. Li and C.-C. Liu, Phys. Rev. B **108**, 205410 (2023).

[68] L. Fu and C. L. Kane, Phys. Rev. B **76**, 045302 (2007).

[69] See Supplemental Material at http://link.aps.org/supplemental/10.1103/PhysRevB.109.L201109 for more detailed information on (I) derivation of the edge Hamiltonian for the Néel vector along an arbitrary direction and the manipulation of the topological corner states by rotating the Néel vector, (II) mirror-graded winding number calculated with Néel vector along $[1\bar{1}]$ direction, (III) the effective Hamiltonian of any boundary for the heterostructure of altermagnets with *g*-wave and *i*-wave as well as *s*-wave spin splitting, (IV) first-principles calculations methods, (V) a devised sandwich structure consisting of a 2D TI and altermagnets, and (VI) *ab initio* tight-binding model for the sandwich structure, (VII) a minimal tight-binding model for the sandwich structure, (VIII) the topological classification of the system is discussed and the second Stiefel-Whitney number w_2 is determined using the Wilson loop method, which includes Refs. [48–50,73–76,83,84,94–100].

[70] M. Meinert, D. Graulich, and T. Matalla-Wagner, Phys. Rev. Appl. **9**, 064040 (2018).

[71] J. Godinho, H. Reichlová, D. Kriegner, V. Novák, K. Olejník, Z. Kašpar, Z. Šobáň, P. Wadley, R. P. Campion, R. M. Otxoa, P. E. Roy, J. Železný, T. Jungwirth, and J. Wunderlich, Nat. Commun. **9**, 4686 (2018).

[72] S. Yu. Bodnar, L. Šmejkal, I. Turek, T. Jungwirth, O. Gomonay, J. Sinova, A. A. Sapozhnik, H.-J. Elmers, M. Kläui, and M. Jourdan, Nat. Commun. **9**, 348 (2018).

[73] A. Bouhon, A. M. Black-Schaffer, and R.-J. Slager, Phys. Rev. B **100**, 195135 (2019).

[74] J. Ahn and B.-J. Yang, Phys. Rev. B **99**, 235125 (2019).

[75] R. Jackiw and C. Rebbi, Phys. Rev. D **13**, 3398 (1976).

[76] D. Bercioux, J. Cayssol, M. G. Vergniory, and M. Reyes Calvo, *Topological Matter: Lectures from the Topological Matter School* (Springer Nature, Switzerland AG, 2018), Chap. 2.3.
[77] Z. Song, C.-C. Liu, J. Yang, J. Han, M. Ye, B. Fu, Y. Yang, Q. Niu, J. Lu, and Y. Yao, NPG Asia Mater. **6**, e147 (2014).
[78] M. Zhou, W. Ming, Z. Liu, Z. Wang, P. Li, and F. Liu, Proc. Natl. Acad. Sci. USA **111**, 14378 (2014).
[79] C.-C. Liu, S. Guan, Z. Song, S. A. Yang, J. Yang, and Y. Yao, Phys. Rev. B **90**, 085431 (2014).
[80] C.-H. Hsu, Z.-Q. Huang, F.-C. Chuang, C.-C. Kuo, Y.-T. Liu, H. Lin, and A. Bansil, New J. Phys. **17**, 025005 (2015).
[81] F. Reis, G. Li, L. Dudy, M. Bauernfeind, S. Glass, W. Hanke, R. Thomale, J. Schäfer, and R. Claessen, Science **357**, 287 (2017).
[82] W. Luo and H. Xiang, Nano Lett. **15**, 3230 (2015).
[83] N. Marzari and D. Vanderbilt, Phys. Rev. B **56**, 12847 (1997).
[84] I. Souza, N. Marzari, and D. Vanderbilt, Phys. Rev. B **65**, 035109 (2001).
[85] J. Alicea, Y. Oreg, G. Refael, F. von Oppen, and M. P. A. Fisher, Nat. Phys. **7**, 412 (2011).
[86] A. Mahmood, W. Echtenkamp, M. Street, J.-L. Wang, S. Cao, T. Komesu, P. A. Dowben, P. Buragohain, H. Lu, A. Gruverman, A. Parthasarathy, S. Rakheja, and C. Binek, Nat. Commun. **12**, 1674 (2021).
[87] I. J. Park, T. Lee, P. Das, B. Debnath, G. P. Carman, and R. K. Lake, Appl. Phys. Lett. **114**, 142403 (2019).
[88] P. Shirazi, M. K. Panduranga, T. Lee, A. Barra, V. Estrada, D. L. Tran, A. E. Sepulveda, and G. P. Carman, Appl. Phys. Lett. **120**, 202405 (2022).
[89] P. Zhang, C.-T. Chou, H. Yun, B. C. McGoldrick, J. T. Hou, K. A. Mkhoyan, and L. Liu, Phys. Rev. Lett. **129**, 017203 (2022).
[90] V. Baltz, A. Manchon, M. Tsoi, T. Moriyama, T. Ono, and Y. Tserkovnyak, Rev. Mod. Phys. **90**, 015005 (2018).
[91] J.-X. Yin, S. H. Pan, and M. Zahid Hasan, Nat. Rev. Phys. **3**, 249 (2021).
[92] B.-L. Wu, A.-M. Guo, Z.-Q. Zhang, and H. Jiang, Phys. Rev. B **106**, 165401 (2022).
[93] M. Ezawa, arXiv:2403.09150.
[94] P. E. Blöchl, Phys. Rev. B **50**, 17953 (1994).
[95] G. Kresse and J. Hafner, Phys. Rev. B **49**, 14251 (1994).
[96] G. Kresse and J. Furthmüller, Phys. Rev. B **54**, 11169 (1996).
[97] J. P. Perdew, K. Burke, and M. Ernzerhof, Phys. Rev. Lett. **77**, 3865 (1996).
[98] H. J. Monkhorst and J. D. Pack, Phys. Rev. B **13**, 5188 (1976).
[99] V. I. Anisimov, J. Zaanen, and O. K. Andersen, Phys. Rev. B **44**, 943 (1991).
[100] S. L. Dudarev, G. A. Botton, S. Y. Savrasov, C. J. Humphreys, and A. P. Sutton, Phys. Rev. B **57**, 1505 (1998).